



Article

# A Modified Version of the RNG $k$ - $\varepsilon$ Turbulence Model for the Scale-Resolving Simulation of Internal Combustion Engines

Vesselin Krassimirov Krastev <sup>1,\*</sup> , Luca Silvestri <sup>2</sup> and Giacomo Falcucci <sup>2,3</sup> 

<sup>1</sup> Department of Economics, Engineering, Society and Business Organization, University of Tuscia, 01100 Viterbo, Italy

<sup>2</sup> Department of Enterprise Engineering “Mario Lucertini”, University of “Tor Vergata”, 00133 Rome, Italy; silvestri.lc@gmail.com (L.S.); giacomo.falcucci@uniroma2.it (G.F.)

<sup>3</sup> John A. Paulson School of Engineering and Applied Sciences, Harvard University, 33 Oxford St., Cambridge, MA 02138, USA

\* Correspondence: v.krastev@unitus.it or v.krastev84@gmail.com

Received: 7 November 2017; Accepted: 6 December 2017; Published: 13 December 2017

**Abstract:** The unsteady and random character of turbulent flow motion is a key aspect of the multidimensional modeling of internal combustion engines (ICEs). A typical example can be found in the prediction of the cycle-to-cycle variability (CCV) in modern, highly downsized gasoline direct injection (GDI) engines, which strongly depends on the accurate simulation of turbulent in-cylinder flow structures. The current standard for turbulence modeling in ICEs is still represented by the unsteady form of Reynold-averaged Navier Stokes equations (URANS), which allows the simulation of full engine cycles at relatively low computational costs. URANS-based methods, however, are only able to return a statistical description of turbulence, as the effects of all scales of motion are entirely modeled. Therefore, during the last decade, scale-resolving methods such as large eddy simulation (LES) or hybrid URANS/LES approaches are gaining increasing attention among the engine-modeling community. In the present paper, we propose a scale-resolving capable modification of the popular RNG  $k$ - $\varepsilon$  URANS model. The modification is based on a detached-eddy simulation (DES) framework and allows one to explicitly set the behavior (URANS, DES or LES) of the model in different zones of the computational domain. The resulting zonal formulation has been tested on two reference test cases, comparing the numerical predictions with the available experimental data sets and with previous computational studies. Overall, the scale-resolved part of the computed flow has been found to be consistent with the expected flow physics, thus confirming the validity of the proposed simulation methodology.

**Keywords:** internal combustion engines; turbulence modeling; RNG; scale-resolving simulation; cycle-to-cycle variability

---

## 1. Introduction

The idea of merging the unsteady Reynolds-averaged Navier Stokes (URANS) and large eddy simulation (LES) techniques for turbulence modeling is not conceptually new [1] and, at present, is generally considered a mature and robust option for some engineering areas, such as turbomachinery and aerospace applications [2,3]. More recently, this class of methods has started receiving more attention from the internal combustion engine (ICE) modeling community [4–12], because of the need for an alternative to standard LES scale-resolving approaches. In fact, although LES has already emerged as a powerful tool for capturing cycle-to-cycle variability (CCV) phenomena and other instantaneous flow features [13–19], there are still some unresolved issues that limit its wider usage

for the design and optimization of reciprocating engines. More specifically, a well-resolved LES would require an extremely fine near-wall mesh, high-order numerical schemes, small time steps (even without combustion) and high-quality computational cells across the whole domain involved in the simulation [13]. Additionally, a significant number of simulated cycles are usually required to extract reliable engine statistics, which makes LES practically unfeasible for industry-grade routine calculations. Therefore, URANS/LES hybrids are being explored as a possible solution for keeping adequate scale-resolving capabilities in the key areas of the computed flow, but mitigating at the same time some of the aforementioned concerns.

One of the most successful hybrid methodologies comes from the application of the detached-eddy-simulation (DES) principle [1,20], which introduces a LES-type scale-resolving potential into a classical, URANS-based modeling foundation. In a series of previous works [10–12], we have already assessed DES-type reformulations of a particular URANS closure called  $k-g$ , which was originally developed for external aerodynamics predictions [21–24]. As a result of the encouraging results obtained, in the present work, we have decided to evaluate a similar reformulation of the RNG  $k-\varepsilon$  model [25], which is often referred to as the de facto standard for the URANS-based simulation of reciprocating engines [26]. Section 2 of the paper is dedicated to the description of the steps required for the model modification, while Section 3 is devoted to the analysis of the here-considered engine-like test cases, which include a stationary intake valve configuration and a reference piston/cylinder assembly. Conclusions and future work proposals are drawn in Section 4.

## 2. Zonal-DES Reformulation of the RNG $k-\varepsilon$ Model

### 2.1. Derivation of the Zonal-DES Form

The standard, compressible form of the RNG  $k-\varepsilon$  URANS model consists of the following transport equations for  $k$  and  $\varepsilon$ :

$$\rho \frac{\partial k}{\partial t} + \nabla \cdot (\rho \mathbf{U}k) = \rho (\mathcal{P} - \varepsilon) + \nabla \cdot \left[ \left( \frac{\mu_t}{\sigma_k} + \mu \right) \nabla k \right] \quad (1)$$

$$\rho \frac{\partial \varepsilon}{\partial t} + \nabla \cdot (\rho \mathbf{U}\varepsilon) = \rho \frac{\varepsilon}{k} (C_{\varepsilon 1} \mathcal{P} - C_{\varepsilon 2} \varepsilon) - \rho R + C_{\varepsilon 3} \rho \varepsilon (\nabla \cdot \mathbf{U}) + \nabla \cdot \left[ \left( \frac{\mu_t}{\sigma_\varepsilon} + \mu \right) \nabla \varepsilon \right] \quad (2)$$

where the dynamic turbulent viscosity is given by:

$$\mu_t = \rho C_\mu \frac{k^2}{\varepsilon} \quad (3)$$

and

$$R = C_\mu \eta^3 \frac{(1 - \eta/\eta_0) \varepsilon^2}{1 + \zeta \eta^3} \frac{1}{k}; \quad \eta = |\mathbf{E}| \frac{k}{\varepsilon} \quad (4)$$

with  $|\mathbf{E}|$  being the magnitude of the mean rate-of-strain tensor, while  $C_\mu$ ,  $C_{\varepsilon 1}$ ,  $C_{\varepsilon 2}$ ,  $\sigma_k$ ,  $\sigma_\varepsilon$ ,  $\zeta$  and  $\eta_0$  are all standard closure constants. The third right-hand-side (RHS) term in Equation (2) accounts for the effects of velocity compression/dilatation on the turbulence dissipation rate and, for realistic engine flows with fuel sprays and combustion, is usually set according to the expression developed by Han and Reitz [26]. In the present work, a simpler choice was made, assuming  $C_{\varepsilon 3}$  equal to  $-0.33$  [27].

A DES model can be obtained from a two-equation URANS closure through a simple modification of the turbulent kinetic-energy sink term  $\mathcal{S}_k$ , namely [28],

$$\mathcal{S}_{k,RANS} = \rho \varepsilon = \rho \frac{k^{3/2}}{l_{RANS}}; \quad l_{RANS} = \frac{k^{3/2}}{\varepsilon} \quad (5)$$

$$\mathcal{S}_{k,DES} = F_{DES} \mathcal{S}_{k,RANS}; \quad F_{DES} = \max \left( \frac{l_{RANS}}{C_{DES} \Delta}, 1 \right) \quad (6)$$

where  $\Delta$  is a spatial filter parameter, usually related to the local grid spacing, and  $C_{DES} \approx \mathcal{O}(1)$ . We note that the  $F_{DES}$  expression is general and can be applied to any URANS model, provided that the  $l_{RANS}$  form is adapted accordingly. Replacing  $S_{k,RANS}$  with  $S_{k,DES}$  generates a standard seamless DES model, where the switching between a RANS-type and a LES-type turbulent viscosity formulation is entirely managed by the model itself. Seamless DES is very efficient in external flows with massive separations [20], whereas its effective application to complex internal flows needs a significant number of adaptations and improvements compared to the baseline formulation shown above. In such cases, a somewhat simpler alternative is represented by the “zonal-DES” (ZDES) approach [29–31], in which different parts of the computational domain are marked a priori by the user as URANS, LES or DES. Our zonal rearrangement of the  $F_{DES}$  function consists of:

$$F_{DES}^* = C_{z1}F_{DES} + (1 - C_{z1})F_{ZDES} \quad (7)$$

$$F_{ZDES} = C_{z2} + (1 - C_{z2}) \left( \frac{l_{RANS}}{C_{DES}\Delta} \right) \quad (8)$$

where  $C_{z1}$  and  $C_{z2}$  are two switching parameters that might be alternatively equal to 0 or 1. Table 1 shows all the possible modes of operation produced by  $F_{DES}^*$ , depending on the different  $C_{z1}$  and  $C_{z2}$  combinations.

**Table 1.** Different modes of the ZDES formulation determined by the  $C_{z1}$  and  $C_{z2}$  values.

$C_{z1}$	$C_{z2}$	Simulation Type	Mode
0	1	URANS	A
1	1/0	DES	B
0	0	LES	C

## 2.2. $C_{DES}$ Constant Calibration

The ZDES model described above has been implemented within the OpenFOAM open-source technology (-dev version, OpenFOAM Foundation [32]), which is based on a collection of C++ object-oriented libraries and tools for computational fluid dynamics (CFD). Similarly to other open-source and commercial CFD solutions aimed at ICE modeling [33–35], the OpenFOAM numerical framework is essentially built on top of a second-order, pressure-based finite-volume methodology.

In any DES-type model, the  $C_{DES}$  constant should be able to provide, in combination with the grid-dependent filter length scale  $\Delta$ , a consistent turbulence energy decay as it operates in LES mode. To determine the optimal  $C_{DES}$  value, energy decay tests have been performed on a homogeneous incompressible turbulence box case, which mimics the experimental measurements of Comte-Bellot and Corrsin [36]. Calculations were carried out on a domain made of  $64^3$  hexahedral cells, using the mode C (pure LES) of the RNG  $k$ - $\epsilon$  model and assuming the cubic root of the cell volume as a spatial filter. The velocity field was initialized through the generalized spectral function found in [37], while temporal integration was performed with a second-order three-point implicit backward scheme. For momentum convection, a low-dissipation filtered central differencing (FCD) scheme [38] was adopted. For  $k$  and  $\epsilon$  being strictly positive quantities, their convective fluxes were interpolated using a second-order bounded linear upwind (LU) scheme.

The results from the  $C_{DES}$  calibration are shown in Figure 1. The predicted three-dimensional energy spectra are assessed at two reference simulation times ( $t = t_1$  and  $t = t_2$ ), which correspond to the two measuring stations in the experiments of Comte-Bellot and Corrsin. Apparently, the optimal value of  $C_{DES}$  is located between 0.65 and 0.5, thus producing  $C_{DES} = 0.55$  as the default option for all the subsequent simulations.

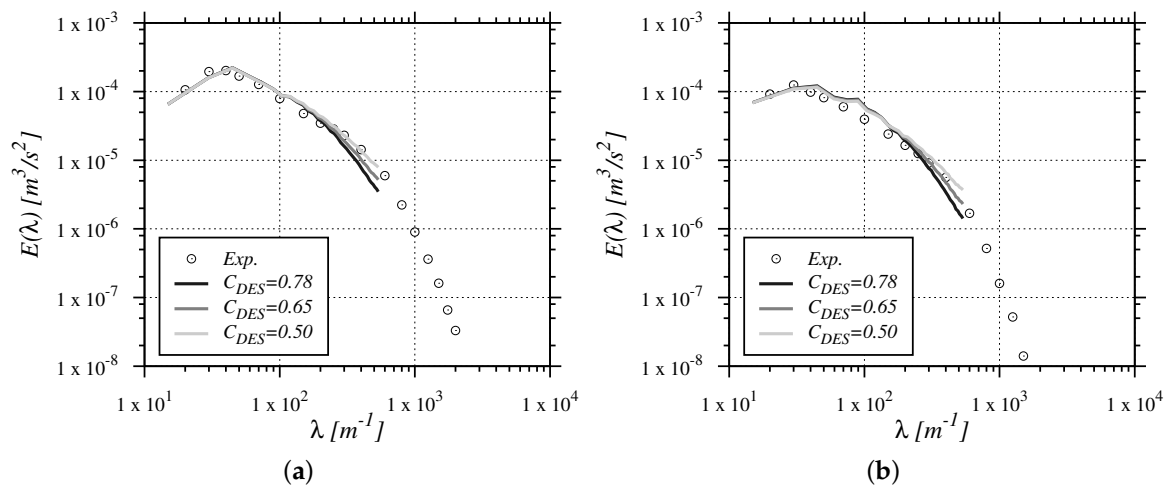


**Figure 1.** Three-dimensional energy spectra obtained with the pure LES mode of the RNG  $k$ - $\epsilon$  model, for different  $C_{DES}$  values: (a)  $t = t_1$ ; (b)  $t = t_2$ .

### 3. Results and Discussion

#### 3.1. Fixed Intake Valve

In spite of its relative simplicity, this case is quite popular among engine CFD modelers [7,10–12,39–41], because of its close resemblance to an actual engine intake flow. Figure 2a sketches the domain configuration, while Table 2 contains the dimensional parameters and flow conditions used for the simulations' setup. Table 3 collects the main features of the two computational grids adopted in the present study (meshes 1 and 2), which were generated through the OpenFOAM built-in snappyHexMesh tool.

The reference experimental flow configuration is essentially incompressible ( $Ma < 0.2$ ); thus the compression/dilatation term in Equation (2) was completely neglected for this case. At the open boundaries, velocity-inlet and pressure-outlet boundary conditions were applied. The momentum flux at the walls was modeled through Spalding's nonlinear function [42], while for  $k$  and  $\epsilon$ , a switching wall function formulation was used [43]. Both standard RANS and ZDES simulations were performed, whereas for ZDES, a mode A/mode C interface was placed at the first separation point upstream of the valve seat (see Figure 2b,c). For momentum convection, the LU scheme was used wherever URANS was applied (mode A), and the FCD scheme was adopted for LES (mode C). No synthetic turbulence generation methods were implemented at the URANS/LES interface, which was in the spirit of the original ZDES methodology [29].

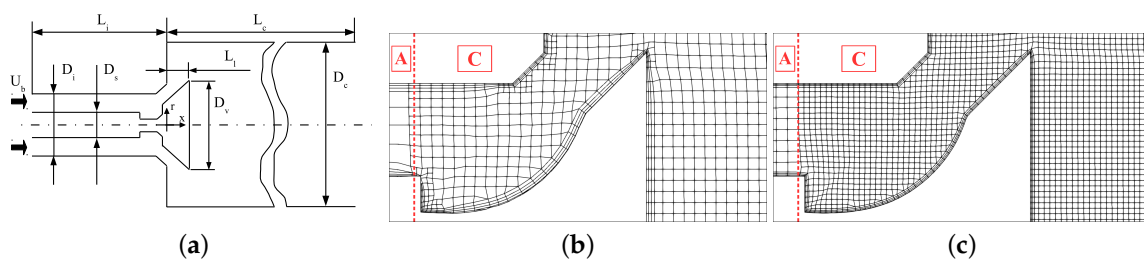


**Figure 2.** Details of the fixed intake valve case: (a) geometrical parameters; (b) axial section of mesh 1 with the ZDES modes subdivision; (c) axial section of mesh 2 with the ZDES modes subdivision.

**Table 2.** Dimensions and flow parameters for the fixed intake valve simulation setup.

Parameter	Value
Valve stem diameter ( $D_s$ )	16 mm
Intake duct diameter ( $D_i$ )	34 mm
Cylinder diameter ( $D_c$ )	120 mm
Valve head diameter ( $D_v$ )	40 mm
Intake duct length ( $L_i$ )	140 mm
Cylinder length ( $L_c$ )	300 mm
Valve lift ( $L_l$ )	10 mm
Inlet bulk velocity ( $U_b$ )	$\approx 60$ m/s
Inlet bulk Reynolds number ( $Re_b$ )	$\approx 3 \times 10^4$

**Table 3.** Main parameters of the computational grids for the fixed intake valve case.

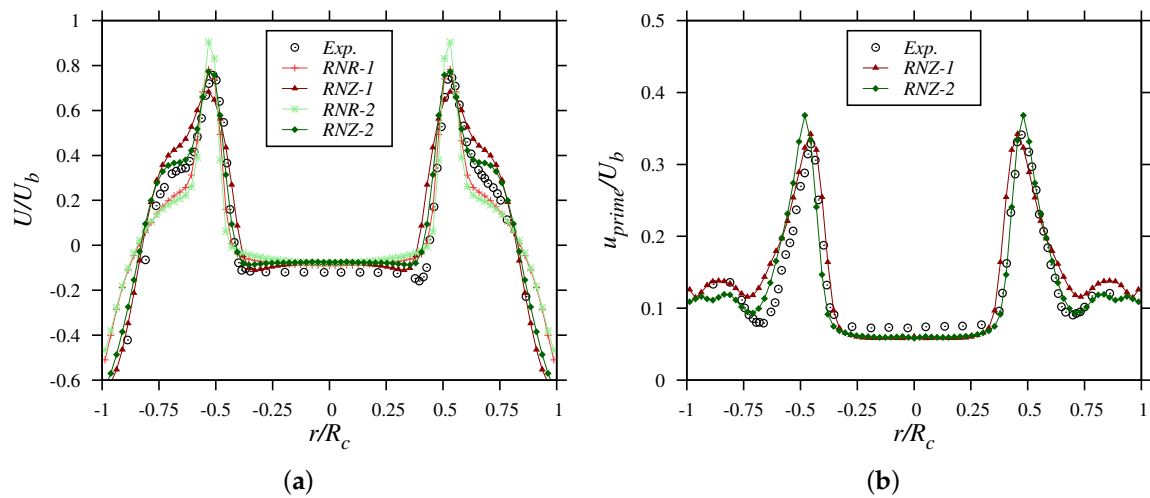
Parameter	Mesh 1	Mesh 2
Total cell number	$0.98 \times 10^6$	$5.9 \times 10^6$
Grid type	unstructured	unstructured
Minimum bulk cell length	1.1 mm	0.56 mm
Maximum bulk cell length	4.5 mm	4.5 mm
Skewness (max)	3.93	4.07
Non-orthogonality (max/avg)	69.2/5.7 deg	69.3/3.2 deg
$y^+$ (max)	$\approx 55$	$\approx 45$

### 3.1.1. Mean Velocity and Root-Mean-Square Fluctuations

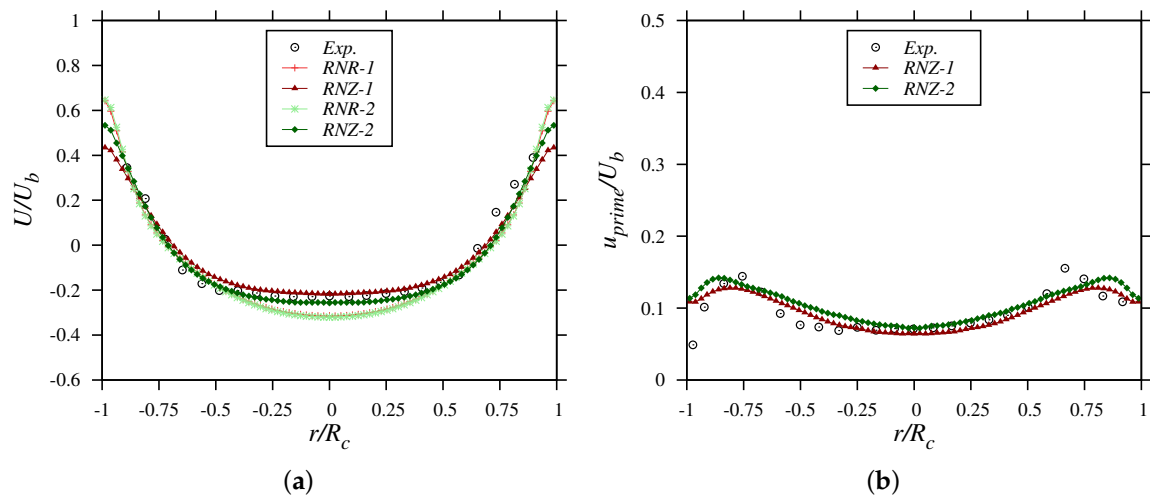
Axial time-averaged velocities and root-mean-square (RMS) axial velocity fluctuations were analyzed at  $x = 20$  mm and  $x = 70$  mm from the head of the cylinder. Converged RANS solutions were used to initialize the ZDES runs, and an initial transient of two flow-through times was considered before starting the statistical monitoring of the resolved fields. The monitoring lasted for an additional five flow-through times, in order to guarantee a sufficient level of statistical convergence. During the unsteady simulations, the maximum convective Courant-Friedrichs-Lewy (CFL) number was limited to 2. We note that steady RANS profiles are marked as *RNR*, while time-resolved ZDES predictions are marked as *RNZ*. An additional 1 or 2 suffix is added to distinguish between predictions obtained with mesh 1 or mesh 2. All results are compared with laser Doppler anemometry (LDA) experimental measurements taken from [39].

Figure 3 displays time-averaged and RMS profiles at  $x = 20$  mm. Mean velocity predictions obtained with mesh 1 show some departures from the experimental values, both for RANS and ZDES. The former better describes the characteristic peak located approximately at  $r/R_c = 0.55$ , whereas the latter is more accurate in the outer recirculation region. On mesh 2, the ZDES results exhibit a very good accordance with the experiments, while there is no clear improvement for RANS. RMS fluctuations were only evaluated for ZDES, as RANS results would have been entirely derived from the modeled turbulent kinetic energy and thus inherently affected by the local isotropy assumption. Figure 3b shows how the scale-resolving capabilities of the ZDES formulation are already significant for the coarser mesh case, confirming also a consistent sensitivity to grid refinement for the resolved part of the flow.

Figure 4 refers to the second considered measuring section, placed at  $x = 70$  mm. At this distance from the head, the mean flow development is dominated by a large central recirculation zone. Mean velocity profiles are well predicted by ZDES, even with the coarser mesh 1 option. The RANS form of the RNG  $k-\epsilon$  model is not able to reproduce the velocity “flattening” close to the cylinder axis, irrespective of the mesh refinement level. Regarding RMS fluctuations, ZDES outcomes from both meshes are still relatively close to each other, with only a slightly higher amount of resolved flow content for mesh 2.



**Figure 3.** Mean and RMS profiles at  $x = 20$  mm: (a) mean axial velocity; (b) RMS axial velocity fluctuation.



**Figure 4.** Mean and RMS profiles at  $x = 70$  mm: (a) mean axial velocity; (b) RMS axial velocity fluctuation.

### 3.1.2. Flow Structures and Axial Pressure Development

The resolution level of ZDES simulations can be qualitatively assessed through the visualization of instantaneous snapshots of pressure isosurfaces, as shown in Figure 5. The characteristic ring-shaped structures generated by the annular jet flow, which have already also been detected in [39], are evident. The mesh 2 pressure isosurface snapshot presents smaller structures with higher vorticity intensities, thus suggesting a broader range of resolved turbulence scales.

For such a flow configuration, the in-cylinder axial pressure development can be divided into four stages [39,40]: a sudden pressure drop induced by the intake jet acceleration, with a minimum located around  $x/R_c \approx 0.25$ ; a pressure peak at  $x/R_c \approx 0.75$ , as a result of the jet impingement on the wall; a second, weaker, pressure drop at  $x/R_c \approx 1$ , originated by the jet rebound; the final pressure recovery, which ends up at about  $x/R_c \approx 2.5$ . As for the isosurfaces in Figure 5, axial profiles are presented in Figure 6 in terms of the nondimensional pressure coefficient  $C_p = 2(p - p_{out})/\rho U_b^2$ , where  $p_{out}$  is the reference pressure value at the cylinder outlet,  $\rho$  is the reference (constant) fluid density and  $U_b$  is the inlet bulk velocity. Neither RANS profiles properly capture the initial drop; they overestimate the pressure peak and produce too slow a recovery after the jet rebound. Conversely, ZDES computations

on mesh 1 return a more consistent description of all the four stages mentioned above. Moving to mesh 2, the agreement between ZDES and the experiments becomes remarkable.

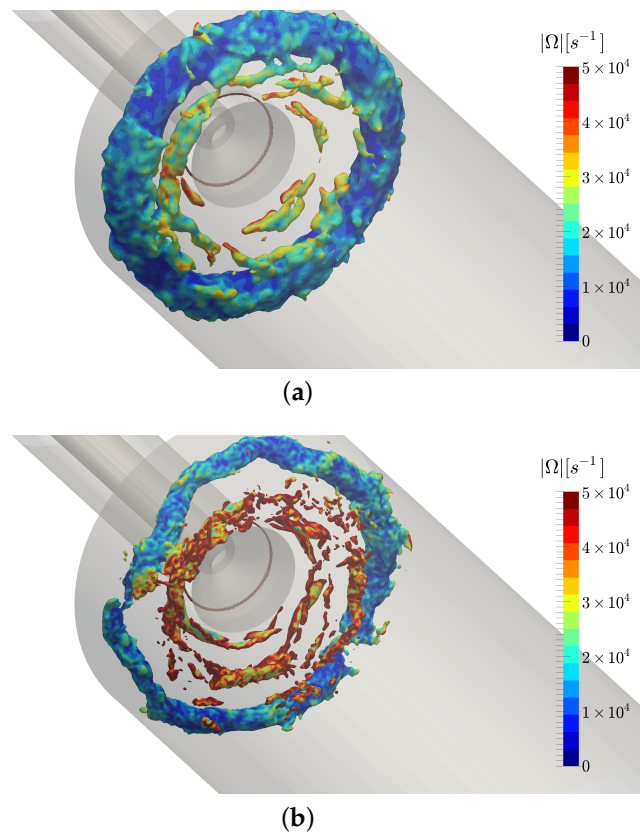


**Figure 5.** Annular flow structures' visualization through instantaneous pressure coefficient isosurfaces ( $C_p = -0.1$ ), colored by vorticity magnitude  $|\Omega|$ : (a) coarse grid; (b) fine grid.

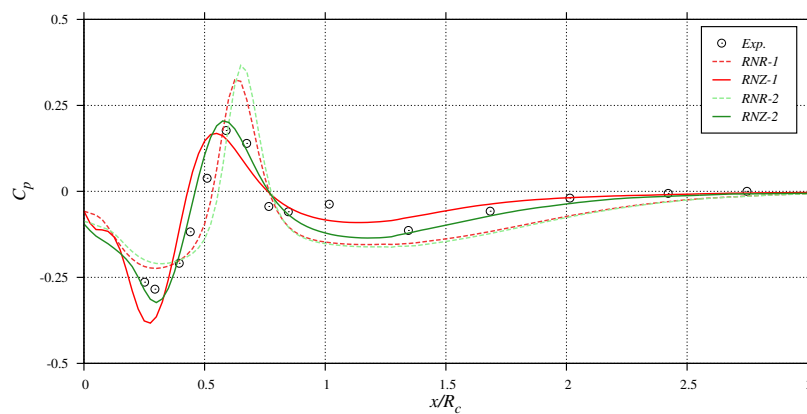


**Figure 6.** In-cylinder pressure coefficient development along the axial direction.

### 3.2. Reciprocating Piston/Cylinder Assembly

Figure 7a and Table 4 show the geometry and dimensions of the piston/cylinder assembly, which follows the experimental configuration found in [44]. The piston motion is purely sinusoidal, with the piston coordinate  $z_p$  and linear velocity  $U_p$  given by:

$$z_p(t) = -2c + \frac{S}{2} \sin(\Omega t) ; \quad U_p(t) = \Omega \frac{S}{2} \cos(\Omega t) \quad (9)$$

with  $\Omega = 2\pi n/60$ . Each motion cycle lasts for 360 crank angle degrees and is made of an intake and an exhaust stroke. A single, coaxial valve is fixed in the open position, so that no effective volumetric compression or expansion occurs. The true computational domain includes also a large plenum upstream of the intake duct (not shown in Figure 7a), which was implemented to avoid complex boundary conditions at the valve gap. A moving-mesh strategy was used to accommodate the piston motion, on the basis of a point-stretching concept [32,45,46]. The domain was divided into two regions: a fixed-mesh zone, which extended up to  $z = -c/3$  mm, and the true moving-mesh zone, which covered the remaining part of the in-cylinder volume (see Figure 7b). Differently from the fixed intake valve case, a block-structured topology was chosen, in order to optimize the grid quality and to effectively control cell stretching in the moving-mesh region. Table 5 shows the key features of the mesh, while Figure 7c shows a visual snapshot of the valve region and of the ZDES modes' distribution.

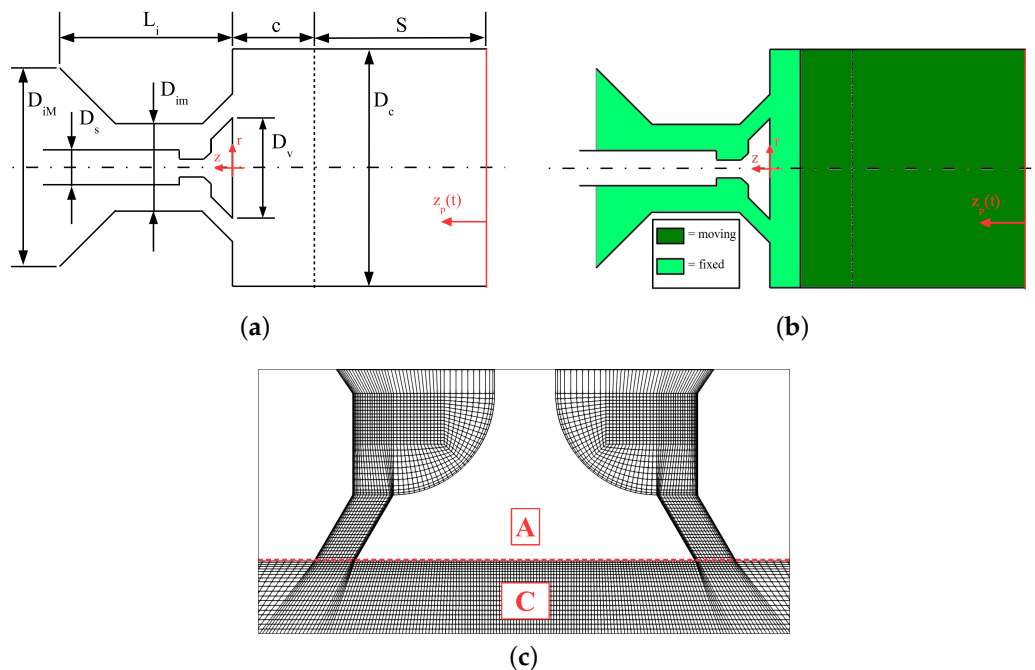


**Figure 7.** Details of the piston/cylinder assembly: (a) geometrical parameters; (b) moving mesh arrangement; (c) axial section of the mesh with the ZDES modes subdivision.

In spite of the very small density variations, a compressible solver formulation was used for this case, to test the proposed ZDES formulation in a more realistic, ICE-oriented computational framework. Subiterations were added to stabilize the pressure–velocity coupling algorithm, while the maximum acoustic CFL number was limited to 0.9. Additionally, the linear upwind stabilized transport (LUST) scheme [7,12,46,47] was used for momentum convection instead of FCD, because of its ability to damp out spurious density oscillations in compressible solvers [38]. The rest of the numerical setup was kept similar to that shown for the steady intake valve case.



**Table 4.** Dimensions and flow parameters for the piston/cylinder simulation setup.

Parameter	Value
Valve stem diameter ( $D_s$ )	6 mm
Intake duct minimum diameter ( $D_{im}$ )	41.6 mm
Intake duct maximum diameter ( $D_{iM}$ )	66 mm
Cylinder diameter ( $D_c$ )	75 mm
Valve head diameter ( $D_v$ )	33.6 mm
Intake duct length ( $L_i$ )	40 mm
Piston stroke ( $S$ )	60 mm
Clearance at TDC ( $c$ )	30 mm
Fluid	Air at standard condition
Piston turning speed ( $n$ )	200 rpm

**Table 5.** Main parameters of the computational grid for the piston/cylinder case.

Parameter	Value
Cell number (total/in-cylinder)	1.81/1.28 $\times 10^6$
Grid type	Block-structured
Axial cell length (in-cylinder)	0.2–0.7 mm
Radial cell length (in-cylinder)	0.4 mm
Azimuthal cell length (in-cylinder)	0.4–2.5 mm
Skewness (max)	1.08
Non-orthogonality (max/avg)	39.9/8 deg
$y^+$ (max)	$\approx 10$

### 3.2.1. Mean Velocity and RMS Fluctuations

To accelerate the statistical convergence of ZDES runs, a combination of azimuthal and ensemble averaging (known also as total averaging) was employed. Previous works have shown that the application of total averaging is able to reduce the cycle count required for convergence up to the order of  $\approx 10$  [12,46]. In our case, 12 cycles were computed, and the first two of them were discarded from the statistical analysis in order to minimize the effects of the initial conditions.

Figures 8–10 compare numerical and experimental [44] profiles of the averaged axial velocity for  $\theta = 36^\circ$ ,  $\theta = 90^\circ$  and  $\theta = 144^\circ$ , at different  $z$  distances from the head of the cylinder. Direct numerical simulation (DNS) data from [46] are also included in the analysis. For  $\theta = 36^\circ$ , the intake flow is in a free-jet configuration rather than a wall-impinging configuration. At this crank angle, averaged velocity predictions from the RNG  $k-\epsilon$  ZDES model are in fairly good agreement with the experiments and reference DNS data. The  $\theta = 90^\circ$  value is considered the most challenging crank angle to simulate for this specific geometry, as a result of the hollow jet reaching its maximum speed and being deflected by the cylinder wall, with the subsequent generation of complex three-dimensional structures. At  $z = 20$  mm, the ZDES profile is qualitatively consistent with the experiments and DNS, but the velocity magnitudes are too low both in the inner (upward-directed) and outer (downward-directed) part of the flow. The results at  $z = 30$  mm are very interesting: on the one hand, DNS is apparently not able to fully reproduce the expected velocity profile, particularly in the near-wall region; on the other hand, predictions from ZDES reproduce the experimental measurements well. For  $\theta = 144^\circ$ , the picture is again similar to that shown for  $\theta = 90^\circ$  and at  $z = -20$  mm, with too low an averaged axial velocity magnitude returned by ZDES over the whole cylinder radius.

RMS axial velocity fluctuations are compared in Figures 11–13. For  $\theta = 36^\circ$  and  $z = -10$  mm, ZDES captures the typical double-peak shape well, but the peak intensities are underestimated with respect to DNS and the experiments. At  $z = -20$  mm, axial fluctuation intensities predicted by ZDES are fairly accurate in the  $0.5 < r/R_c < 0.75$  range, while they appear underestimated elsewhere. The issues related to the  $\theta = 90^\circ$  configuration are confirmed by Figure 12, which shows a significant

deficit of resolved axial fluctuations for  $r/R_c > 0.5$ . Moving to  $\theta = 144^\circ$ , the deficit seems to be largely recovered, particularly at  $z = -20$  mm, while it still persists at  $z = -30$  mm and for  $0.5 < r/R_c < 0.75$ .

Overall, the ZDES results are in reasonable agreement with DNS, given also the relative simplicity of the proposed modeling approach. The reasons for the discrepancies between the two numerical data sets are most likely linked to the transitional (i.e., not fully turbulent) nature of the flow for this particular configuration, which is quite difficult to predict with standard LES-type models [45,46].

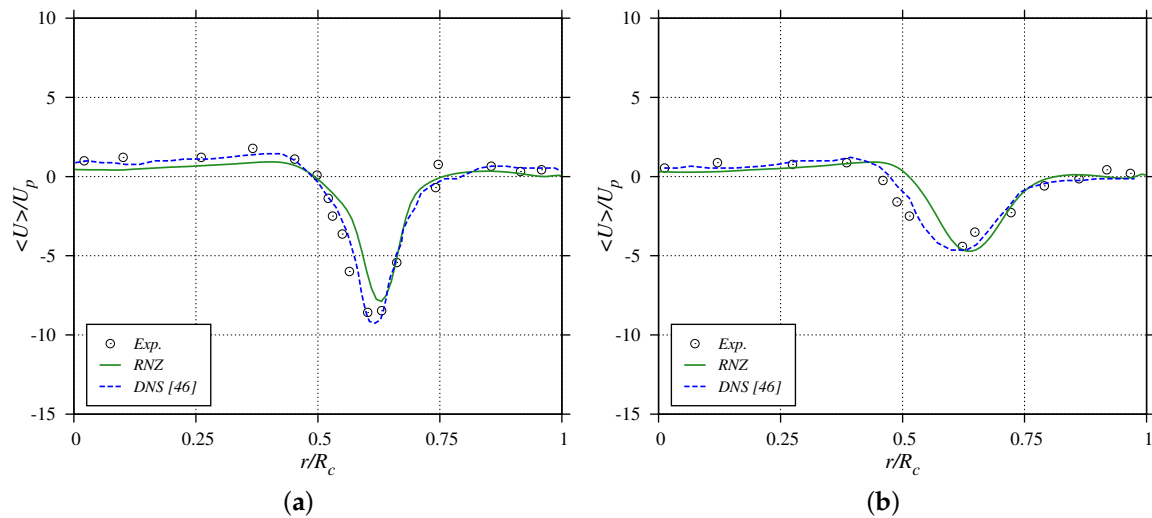


**Figure 8.** Radial distribution of the averaged axial velocity  $\langle U \rangle$  at  $\theta = 36^\circ$ : (a)  $z = -10$  mm; (b)  $z = -20$  mm.

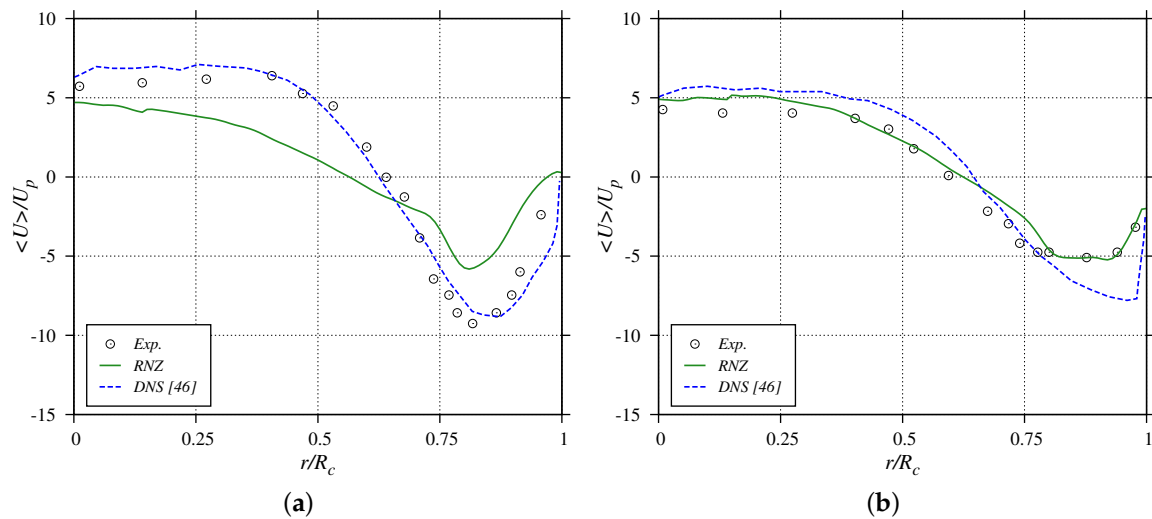


**Figure 9.** Radial distribution of the averaged axial velocity  $\langle U \rangle$  at  $\theta = 90^\circ$ : (a)  $z = -20$  mm; (b)  $z = -30$  mm.

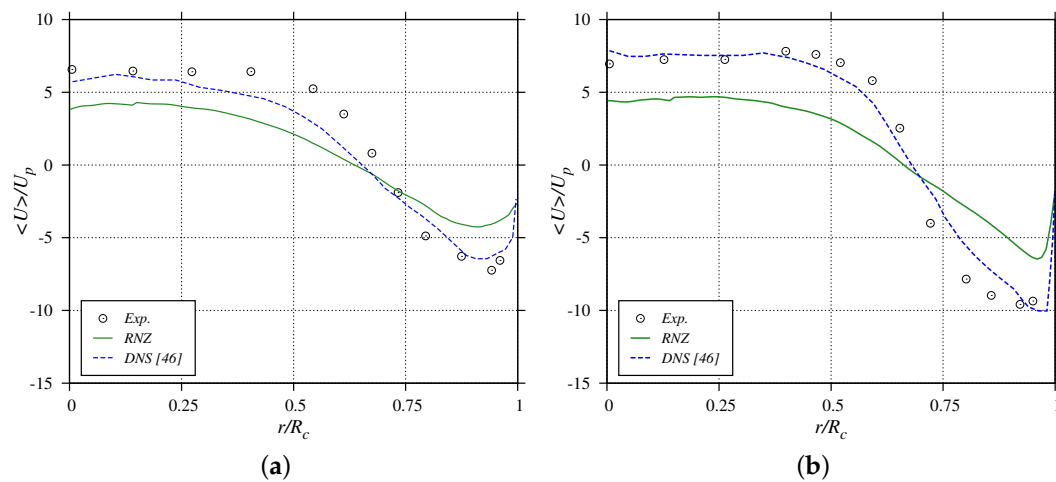


**Figure 10.** Radial distribution of the averaged axial velocity  $\langle U \rangle$  at  $\theta = 144^\circ$ : (a)  $z = -20$  mm; (b)  $z = -30$  mm.

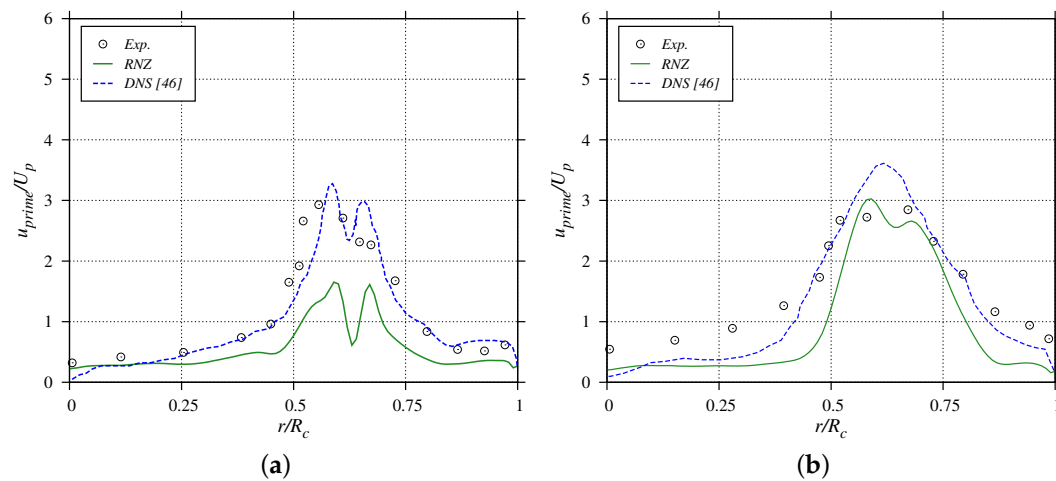


**Figure 11.** Radial distribution of the RMS axial velocity fluctuation  $u_{prime}$  at  $\theta = 36^\circ$ : (a)  $z = -10$  mm; (b)  $z = -20$  mm.

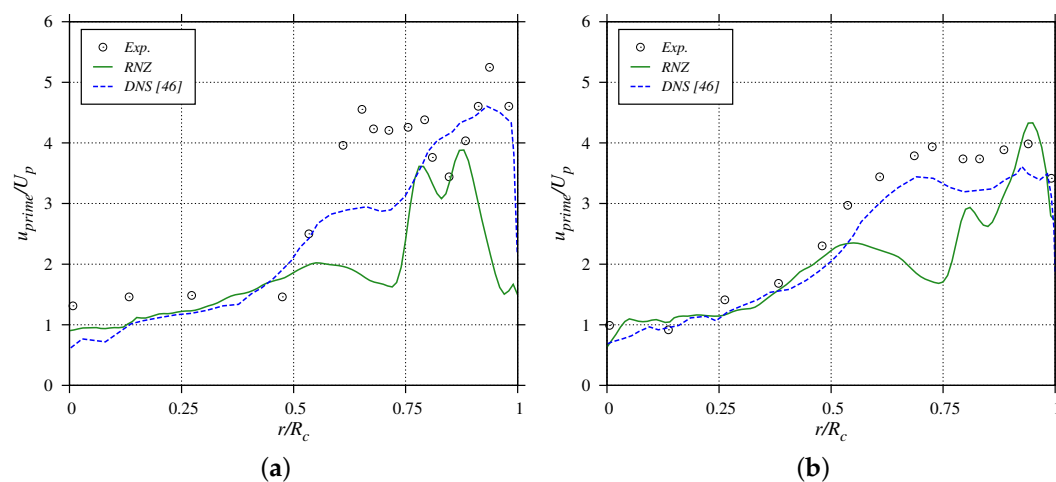


**Figure 12.** Radial distribution of the RMS axial velocity fluctuation  $u_{prime}$  at  $\theta = 90^\circ$ : (a)  $z = -20$  mm; (b)  $z = -30$  mm.

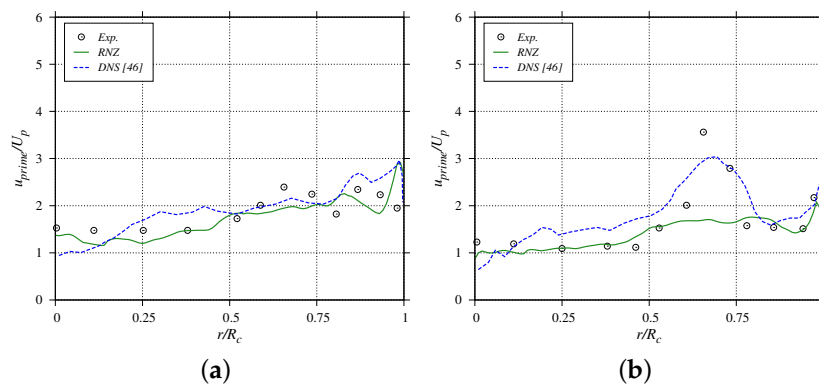


**Figure 13.** Radial distribution of the RMS axial velocity fluctuation  $u_{prime}$  at  $\theta = 144^\circ$ : (a)  $z = -20$  mm; (b)  $z = -30$  mm.

### 3.2.2. Flow Structures and Cycle-to-Cycle Variability

Instantaneous snapshots of the in-cylinder resolved flow content during an intake stroke are shown in Figure 14. For  $\theta = 36^\circ$ , the ring-shaped rolling structure generated by the accelerating intake jet is clearly distinguishable. For  $\theta = 90^\circ$ , the jet impingement and deflection produce an upward-directed stream of flow structures in the inner part of the cylinder, whereas the initial axisymmetric shear layer is still partially visible. The  $\theta = 144^\circ$  configuration is characterized by a pressure rise due to the piston slow-down towards the bottom dead center (BDC), while a wide range of resolved scales covers the entire in-cylinder volume. For this case, CCV was evaluated as already shown in [12,46], through the definition of the volume-averaged velocity magnitude:

$$|\mathbf{V}_{avg}|(\theta) = \frac{1}{\Sigma_c} \int_{\Sigma_c} |\mathbf{V}|(x, y, z, \theta) d\Sigma \quad (10)$$

with  $\Sigma_c$  being the in-cylinder volume and  $\mathbf{V}$  being the velocity vector. The trend of  $|\mathbf{V}|_{avg}$  over six consecutive cycles is shown in Figure 15a. The results from ZDES are superimposed to wall-adapting local eddy viscosity (WALE) LES results from [46]. The overall cycle trends are comparable, but with higher  $|\mathbf{V}|_{avg}$  peaks for ZDES. Figure 15b focuses on the intake stroke variability, evidencing a significant amount of CCV for the peak values, which are located approximately at  $95^\circ$  for both ZDES and reference LES data. Figure 16 adds some basic statistical information about the  $|\mathbf{V}|_{avg}$  peaks. Notably, the cycle-averaged peak value predicted by ZDES is about 10% higher compared to LES, while the relative peak variability across cycles is similar.

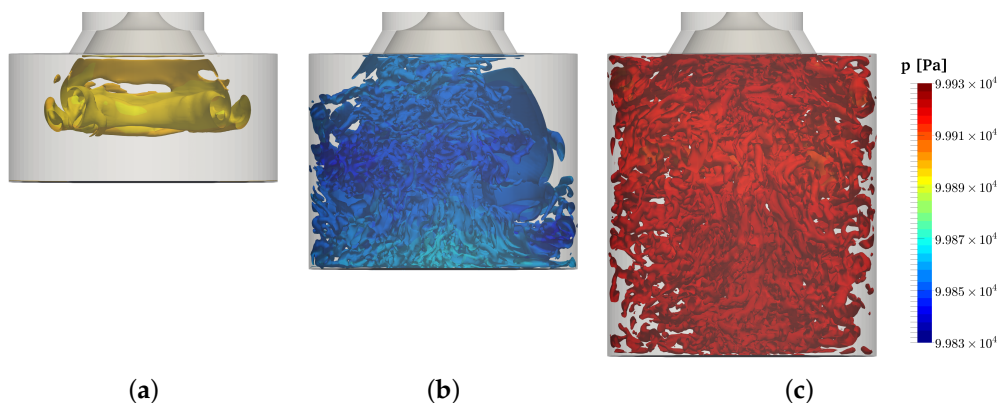


**Figure 14.** Q-criterion realization of the in-cylinder flow structures during an intake stroke: (a)  $\theta = 36^\circ$ ; (b)  $\theta = 90^\circ$ ; (c)  $\theta = 144^\circ$ .

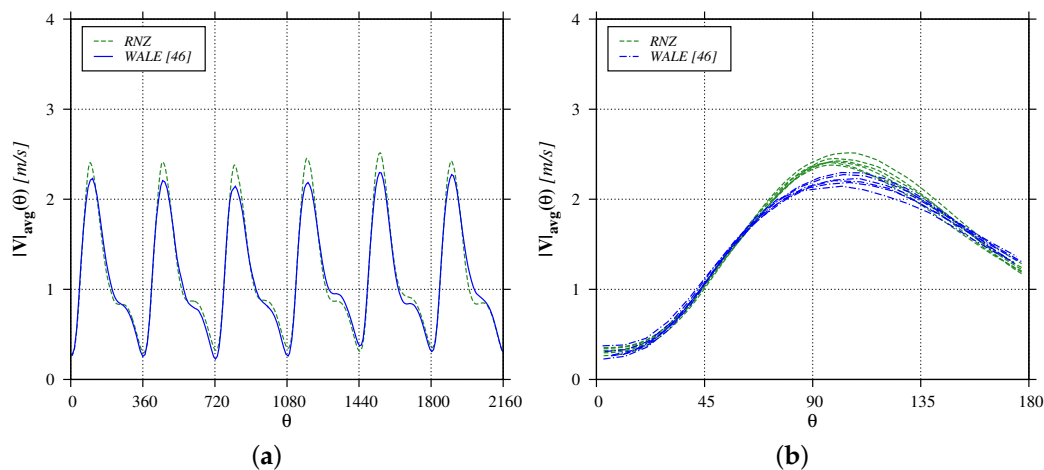


**Figure 15.** Details of CCV in terms of the volume-averaged in-cylinder velocity magnitude: (a) evolution of six consecutive cycles; (b) intake stroke variability.

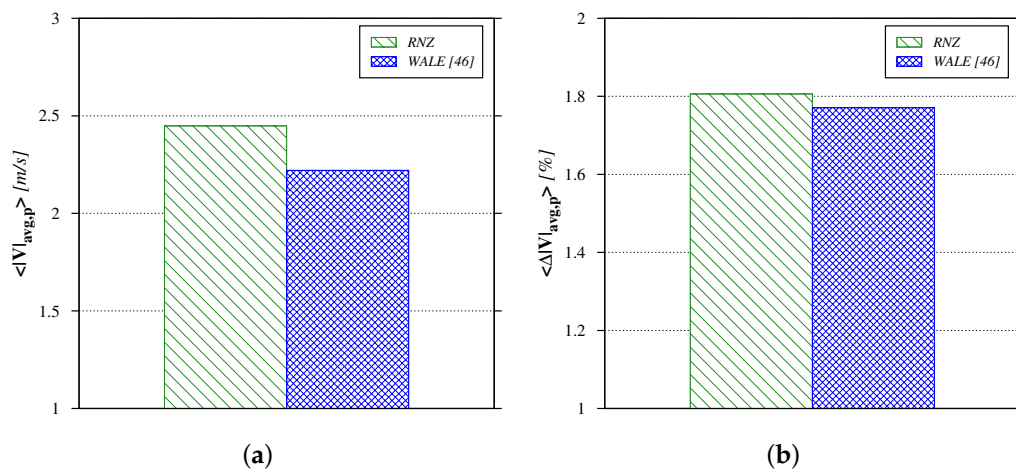


**Figure 16.** Statistical analysis of the  $|V|_{\text{avg}}$  peak value over 20 consecutive cycles: (a) cycle-averaged peak value; (b) cycle-averaged percentage deviation of the peak value.

#### 4. Conclusions

The present work is mainly aimed at the assessment of a ZDES-type modification of the RNG  $k-\epsilon$  turbulence model, for the CFD simulation of ICES. The analysis was based on two canonical test cases, a steady intake valve configuration and a reciprocating piston/cylinder assembly.

The results from the fixed intake valve case highlight the significant level of improvement offered by the proposed ZDES formulation, compared to the standard URANS RNG  $k-\epsilon$  form. More specifically, mean flow parameters are predicted with better accuracy, and a remarkable scale-resolving capability is evidenced in the key regions of the flow, even on relatively coarse computational grids. Furthermore, such capability has been achieved without the need for complex turbulence-generating boundary conditions.

The results from the reciprocating flow case are less clear to interpret. The proposed ZDES model was able to return a rich resolved flow content in the LES-treated part of the domain, but not all of the flow characteristics were properly captured. An explanation for this might come from the relatively low speed regime of the piston/cylinder assembly, which cannot be regarded as a fully turbulent flow configuration. This is in contrast with the LES mode calibration process of any DES/ZDES approach, which is commonly made on boxes of isotropic, high-Reynolds-number turbulence, as for any standard Smagorinsky-type algebraic LES formulation. Moreover, the lack of synthetic turbulence

injection at the URANS-to-LES interface is generally assumed to be acceptable only if the upcoming flow momentum is sufficiently strong to promote the fast growth of resolved flow instabilities.

On the basis of the above considerations, we argue that the proposed modification of the RNG  $k$ - $\varepsilon$  model should be further evaluated under more realistic, high-speed engine flow conditions, including the coupling with additional submodels for spray injection and combustion. Effects of the specific wall treatment should be also considered, as this aspect was not thoroughly investigated in the present work.

**Acknowledgments:** The authors would like to thank Federico Piscaglia for providing accurate geometrical parameters and reference data for the poppet valve and piston/cylinder assembly cases. All the RNG  $k$ - $\varepsilon$  (RANS and ZDES) simulations were performed on the Zeus HPC facility, at the University of Naples "Parthenope". The Zeus facility has been realized through the Italian Government Grant PAC01 00119 MITO—Informazioni Multimediali per Oggetti Territoriali, with Elio Jannelli as the Scientific Responsible. This research has been partially supported by the Italian Ministry Program PRIN, grant no. 20154EHYW9: Combined numerical and experimental methodology for fluid structure interaction in free surface flows under impulsive loading, with Chiara Biscarini as the principal investigator.

**Author Contributions:** Vesselin Krassimirov Krastev and Giacomo Falcucci designed and performed the numerical simulations reported in the paper; Luca Silvestri performed statistical post-processing of the numerical results with *ad hoc* designed Python tools; Vesselin Krassimirov Krastev wrote the paper.

**Conflicts of Interest:** The authors declare no conflict of interest.

## Abbreviations

The following abbreviations are used in this manuscript:

BDC	Bottom dead center
CCV	Cycle-to-cycle variability
CFD	Computational fluid dynamics
CFL	Courant–Friedrichs–Lewy number
DES	Detached-eddy simulation
DNS	Direct numerical simulation
FCD	Filtered central differencing
ICE	Internal combustion engine
LDA	Laser Doppler anemometry
LES	Large-eddy simulation
LUST	Linear upwind stabilized transport
RANS	Reynolds-averaged Navier–Stokes equations
RMS	Root-mean-square
RNG	Re-normalization group
TDC	Top dead center
URANS	Unsteady-RANS
WALE	Wall-adaptive local eddy viscosity
ZDES	Zonal-DES

## References

1. Spalart, P.R.; Wou, W.H.; Strelets, M.; Allmaras, S.R. Comments on the feasibility of LES for wings, and on a hybrid RANS/LES approach. In *Advances in DNS/LES*; Liu, C., Liu, Z., Eds.; Greyden Press: Columbus, OH, USA, 1997; pp. 137–147.
2. Tucker, P.G. Computation of unsteady turbomachinery flows: Part 2—LES and hybrids. *Prog. Aerosp. Sci.* **2011**, *47*, 546–569, doi:10.1016/j.paerosci.2011.07.002.
3. Tucker, P.G.; DeBonis, J.R. Aerodynamics, computers and the environment. *Philos. Trans. R. Soc. A* **2014**, *372*, doi:10.1098/rsta.2013.0331.
4. Buhl, S.; Hartmann, F.; Hasse, C. Identification of large-scale structure fluctuations in IC engines using POD-based conditional averaging. *Oil Gas Sci. Technol.* **2016**, *71*, 1, doi:10.2516/ogst/2015021.

5. Buhl, S.; Dietzsch, F.; Buhl, C.; Hasse, C. Comparative study of turbulence models for scale-resolving simulations of internal combustion engine flows. *Comput. Fluids* **2017**, *156*, 66–80, doi:10.1016/j.compfluid.2017.06.023.
6. Buhl, S.; Hain, D.; Hartmann, F.; Hasse, C. A comparative study of intake and exhaust port modeling strategies for scale-resolving engine simulations. *Int. J. Engine Res.* **2017**, in press, doi:10.1177/1468087417707452.
7. Piscaglia, F.; Montorfano, A.; Onorati, A. A scale adaptive filtering technique for turbulence modeling of unsteady flows in IC engines. *SAE Int. J. Engines* **2015**, *8*, 426–436, doi:10.4271/2015-01-0395.
8. Hasse, C.; Sohm, V.; Durst, B. Detached Eddy Simulation of cyclic large scale fluctuations in a simplified engine setup. *Int. J. Heat Fluid Flow* **2009**, *30*, 32–43, doi:10.1016/j.ijheatfluidflow.2008.10.001.
9. Hasse, C.; Sohm, V.; Durst, B. Numerical investigation of cyclic variations in gasoline engines using a hybrid URANS/LES modeling approach. *Comput. Fluids* **2010**, *39*, 25–48, doi:10.1016/j.compfluid.2009.07.001.
10. Krastev, V.K.; Bella, G.; Campitelli, G. *Some Developments in DES Modeling for Engine Flow Simulation*; SAE Paper 2015-24-2414; SAE International: Warrendale, PA, USA, 2015, doi:10.4271/2015-24-2414.
11. Krastev, V.K.; Bella, G. A Zonal Turbulence Modeling Approach for ICE Flow Simulation. *SAE Int. J. Engines* **2016**, *9*, 1425–1436, doi:10.4271/2016-01-0584.
12. Krastev, V.K.; Silvestri, L.; Falcucci, G.; Bella, G. *A Zonal-LES Study of Steady and Reciprocating Engine-Like Flows Using a Modified Two-Equation DES Turbulence Model*; SAE Paper 2017-24-0030; SAE International: Warrendale, PA, USA, 2017.
13. Rutland, C.J. Large-eddy simulations for internal combustion engines—A review. *Int. J. Engine Res.* **2011**, *12*, 421–451, doi:10.1177/1468087411407248.
14. Granet, V.; Vermorel, O.; Lacour, C.; Enaux, B.; Dugué, V.; Poinot, T. Large-Eddy Simulation and experimental study of cycle-to-cycle variations of stable and unstable operating points in a spark ignition engine. *Combust. Flame* **2012**, *159*, 1562–1575, doi:10.1016/j.combustflame.2011.11.018.
15. Fontanesi, S.; Paltrinieri, S.; D’Adamo, A.; Cantore, G.; Rutland, C. Knock tendency prediction in a high performance engine using LES and tabulated chemistry. *SAE Int. J. Fuels Lubr.* **2013**, *6*, 98–118, doi:10.4271/2013-01-1082.
16. Baumann, M.; Di Mare, F.; Janicka, J. On the validation of Large Eddy Simulation applied to internal combustion engine flows part II: Numerical analysis. *Flow Turbul. Combust.* **2014**, *92*, 299–317, doi:10.1007/s10494-013-9472-x.
17. Fontanesi, S.; Paltrinieri, S.; D’Adamo, A.; Duranti, S. Investigation of Boundary Condition and Field Distribution Effects on the Cycle to Cycle Variability of a Turbocharged GDI Engine Using LES. *Oil Gas Sci. Technol.* **2014**, *69*, 107–128, doi:10.2516/ogst/2013142.
18. Fontanesi, S.; D’Adamo, A.; Rutland, C.J. Large-Eddy Simulation analysis of spark configuration effect on cycle-to-cycle variability of combustion and knock. *Int. J. Engine Res.* **2015**, *16*, 403–418, doi:10.1177/1468087414566253.
19. Truffin, K.; Angelberger, C.; Richard, S.; Pera, C. Using large-eddy simulation and multivariate analysis to understand the sources of combustion cyclic variability in a spark-ignition engine. *Combust. Flame* **2015**, *162*, 4371–4390, doi:10.1016/j.combustflame.2015.07.003.
20. Spalart, P.R. Detached-Eddy Simulation. *Annu. Rev. Fluid Mech.* **2009**, *41*, 181–202, doi:10.1146/annurev.fluid.010908.165130.
21. Kalitzin, G.; Gould, A.R.B.; Benton, J.J. *Application of Two-Equation Turbulence Models in Aircraft Design*; AIAA Paper 96-0327; American Institute of Aeronautics and Astronautics, Inc.: Reston, VA, USA, 1996, doi:10.2514/6.1996-327.
22. Bella, G.; Krastev, V.K. On the RANS Modeling of Turbulent Airflow Over a Simplified Car Model. In Proceedings of the ASME-JSME-KSME 2011 Joint Fluids Engineering Conference: Volume 1, Symposia—Parts A, B, C, and D, Hamamatsu, Japan, 24–29 July 2011; pp. 871–883, doi:10.1115/AJK2011-23006.
23. Krastev, V.K.; Bella, G. *On the Steady and Unsteady Turbulence Modeling in Ground Vehicle Aerodynamic Design and Optimization*; SAE Paper 2011-24-0163; SAE International: Warrendale, PA, USA, 2011, doi:10.4271/2011-24-0163.
24. Krastev, V.K.; Bella, G. High reynolds number hybrid RANS/LES modeling with turbulent time scale bounding. *AIP Conf. Proc.* **2015**, *1648*, 320003, doi:10.1063/1.4912569.
25. Yakhot, V.; Thangam, S.; Gatski, T.B.; Orszag, S.A.; Speziale, C.G. Development of turbulence models for shear flows by a double expansion technique. *Phys. Fluids A* **1992**, *4*, 1510–1520, doi:10.1063/1.858424.

26. Han, Z.; Reitz, R.D. Turbulence Modeling of Internal Combustion Engines Using RNG  $k$ - $\epsilon$  Models. *Combust. Sci. Technol.* **1995**, *106*, 267–295, doi:10.1080/00102209508907782.
27. El Tahry, S.H.  $k$ - $\epsilon$  Equation for Compressible Reciprocating Engine Flows. *J. Energy* **1983**, *7*, 345–353, doi:10.2514/3.48086.
28. Travin, A.; Shur, M.L.; Strelets, M.; Spalart, P.R. Physical and Numerical Upgrades in the Detached-Eddy Simulation of Complex Turbulent Flows. In *Advances in LES of Complex Flows*; Friedrich, R., Rodi, W., Eds.; Kluwer Academic Publishers: Dordrecht, The Netherlands, 2002; pp. 239–254.
29. Deck, S. Zonal-Detached-Eddy Simulation of the Flow Around a High-Lift Configuration. *AIAA J.* **2005**, *43*, 2372–2384, doi:10.2514/1.16810.
30. Deck, S. Recent improvements in the Zonal Detached Eddy Simulation (ZDES) formulation. *Theor. Comput. Fluid Dyn.* **2012**, *26*, 523–550, doi:10.1007/s00162-011-0240-z.
31. Deck, S.; Gand, F.; Brunet, V.; Ben Khelil, S. High-fidelity simulations of unsteady civil aircraft aerodynamics: Stakes and perspectives. Application of zonal detached eddy simulation. *Philos. Trans. R. Soc. A* **2014**, *372*, doi:10.1098/rsta.2013.0325.
32. The OpenFOAM Foundation. User Guide. Available online: <https://cfd.direct/openfoam/user-guide/> (accessed on 7 November 2017).
33. Torres, D.J.; Trujillo, M.F. KIVA-4: An unstructured ALE code for compressible gas flow with sprays. *J. Comput. Phys.* **2006**, *219*, 943–975, doi:10.1016/j.jcp.2006.07.006.
34. *STAR-CD Methodology Version 4.28*; Siemens Product Lifecycle Management Inc.: Plano, TX, USA, 2017.
35. *CONVERGE 2.3 Theory Manual*; Convergent Science Inc.: Madison, WI, USA, 2017.
36. Comte-Bellot, G.; Corrsin, S. Simple Eulerian time correlation of full and narrow-band velocity signals in grid-generated, ‘isotropic’ turbulence. *J. Fluid Mech.* **1971**, *48*, 273–337, doi:10.1017/S0022112071001599.
37. Knaepen, B.; Debliquy, O.; Carati, D. DNS and LES of a shear-free mixing layer. In *Center for Turbulence Research, Annual Research Briefs*; Stanford University: Stanford, CA, USA, 2003; pp. 307–318.
38. Lysenko, D.A.; Ertesvåg, I.S.; Rian, K.E. Large-Eddy Simulation of the Flow Over a Circular Cylinder at Reynolds Number  $2 \times 10^4$ . *Flow Turbul. Combust.* **2014**, *92*, 673–698, doi:10.1007/s10494-013-9509-1.
39. Thobois, L.; Rymer, G.; Soulères, T.; Poinot, T. *Large-Eddy Simulation in IC Engine Geometries*; SAE Paper 2004-01-1854; SAE International: Warrendale, PA, USA, 2004, doi:10.4271/2004-01-1854.
40. Thobois, L.; Rymer, G.; Soulères, T.; Poinot, T. Large-eddy simulation for the prediction of aerodynamics in IC engines. *Int. J. Veh. Des.* **2005**, *39*, 368–382, doi:10.1504/IJVD.2005.008468.
41. Piscaglia, F.; Montorfano, A.; Onorati, A.; Brusiani, F. Boundary Conditions and SGS Models for LES of Wall-Bounded Separated Flows: An Application to Engine-Like Geometries. *Oil Gas Sci. Technol.* **2014**, *69*, 11–27, doi:10.2516/ogst/2013143.
42. Spalding, D.B. A single formula for the law of the wall. *J. Appl. Mech.* **1961**, *28*, 439–446, doi:10.1115/1.3641728.
43. Kalitzin, G.; Medic, G.; Iaccarino, G.; Durbin, P. Near-wall behavior of RANS turbulence models and implications for wall functions. *J. Comput. Phys.* **2004**, *204*, 265–291, doi:10.1016/j.jcp.2004.10.018.
44. Morse, A.P.; Whitelaw, J.H.; Yanneskis, M. Turbulent flow measurements by laser-doppler anemometry in motored piston-cylinder assemblies. *J. Fluids Eng.* **1979**, *101*, 208–216, doi:10.1115/1.3448937.
45. Piscaglia, F.; Montorfano, A.; Onorati, A. Towards the LES simulation of IC engines with parallel topologically changing meshes. *SAE Int. J. Engines* **2013**, *6*, 926–940, doi:10.4271/2013-01-1096.
46. Montorfano, A.; Piscaglia, F.; Schmitt, M.; Wright, Y.M.; Frouzakis, C.E.; Tomboulides, A.G.; Boulouchos, K.; Onorati, A. Comparison of Direct and Large-Eddy Simulations of the turbulent flow in a valve/piston assembly. *Flow Turbul. Combust.* **2015**, *95*, 461–480, doi:10.1007/s10494-015-9620-6.
47. Weller, H. Controlling the computational modes of the arbitrarily structured C grid. *Mon. Weather Rev.* **2012**, *140*, 3220–3234, doi:10.1175/MWR-D-11-00221.1.

